RESEARCH ARTICLE

In-flight measurement of free-stream turbulence in the convective boundary layer

Michael Greiner[1] [iD] · Werner Würz[1]

Abstract

Natural laminar flow airfoils have achieved such a level of refinement that further optimisation and subsequent wind tunnel testing need to regard the specific free-stream turbulence to be expected during operation. This requires the characterisation of this turbulence in terms of those properties which are relevant for boundary layer receptivity and subsequent transition. These parameters of turbulence change with environmental conditions and, in case of aircraft, along the flight profile. This study investigates the free-stream turbulence relevant for the case of sailplane airfoils. In-flight measurements with a constant temperature anemometer x-wire probe were conducted during cross-country flights in Central Europe and provided 22 h of flight data, covering thermalling phases as well as straight flight legs. Longitudinal and transversal velocity fluctuations were recorded well into the dissipation range. The special challenges of operating a constant temperature anemometer probe continuously for several hours are addressed. The permanent unsteadiness of the inflow poses challenges for the evaluation, but also provides a broad database of measured turbulence levels. The quality of the measurements is shown by verifying some of the predictions of Kolmogorov's inertial range theories. Free-stream turbulence in thermalling phases is sufficiently homogeneous to be described accurately, as the dissipation range fluctuates only in a limited range and follows a log-normal distribution. On the straight flight legs, the turbulence depends on the convective activity along the flight path. In general, within the convective part of the atmosphere, turbulence levels are found to be significantly larger than in low-turbulence wind tunnels.

✉ Michael Greiner
michael.greiner@iag.uni-stuttgart.de

[1] Institute of Aerodynamics and Gas Dynamics, University of Stuttgart, 70550 Stuttgart, Germany

Graphical abstract
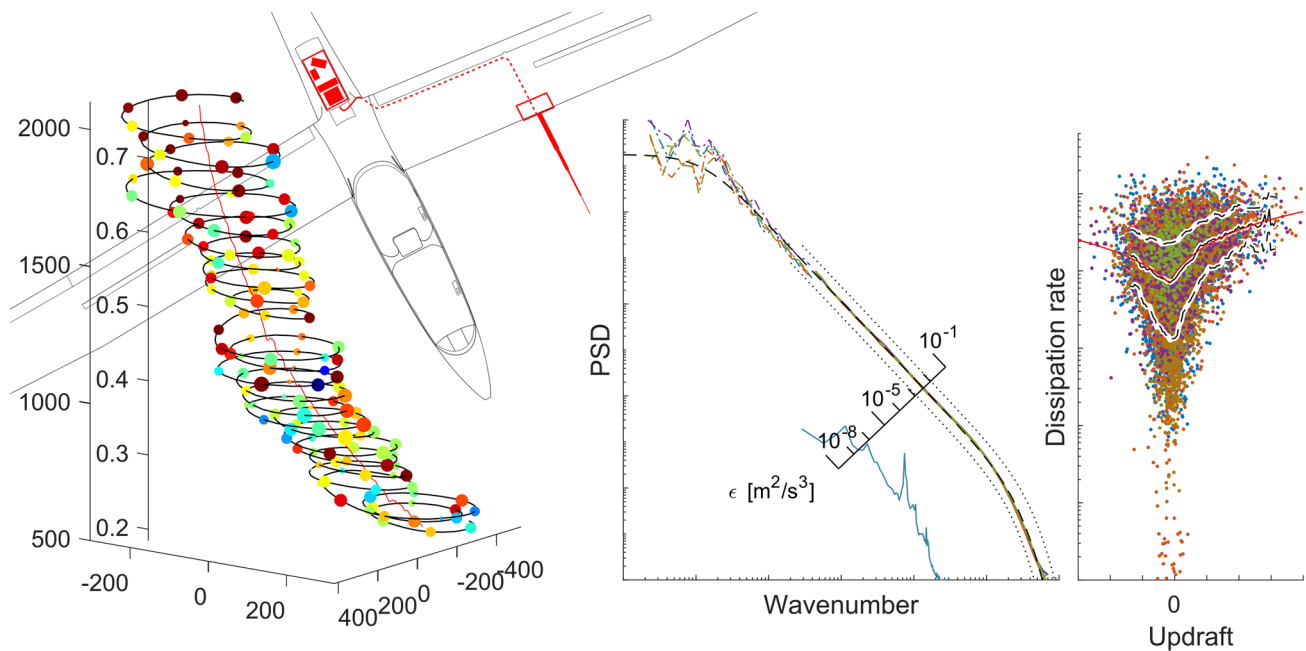
1 Introduction

The use of natural laminar flow (NLF) airfoils is state of the art on sailplanes and wind turbines and becomes increasingly common in general aviation. The low drag of NLF-airfoils contributes considerably to the performance gains achieved in these products. The favourable drag values are linked to the retarded laminar to turbulent transition in the boundary layer. Under 2D conditions and in a low-turbulence environment, this transition process is dominated by the exponential amplification of Tollmien–Schlichting (TS) waves, which can be modelled to predict transition. The e^n criterion (Smith and Gamberoni 1956; van Ingen 1956) delivers reliable transition locations and is a standard method in airfoil design (Drela 1989).

A remaining problem is the prediction of the transition location at increased levels of free-stream turbulence (FST). NLF-airfoils are generally developed for, and wind tunnel tested under calm conditions, but it is known that some sailplanes experience a loss of performance when entering turbulent air (Bertolotti 2001; Peltzer 2008). While on one side the range of favourable angle of attacks may become narrower (Reeh 2014), on the other side laminar separation bubbles may be impaired (Balzer and Fasel 2016). The kind of operation plays a role, as pilots of powered airplanes generally avoid turbulence (Pearson

and Sharman 2017), whereas sailplane pilots are seeking turbulent thermals in convective atmospheric boundary layers.

As a first approach, the e^n criterion was empirically adopted to the turbulence levels achieved in wind tunnels (Mack 1977; van Ingen 1977; Crouch 2008). However, difficulties remain using this approach in general, e.g. when applying it on different airfoils (Romblad et al. 2018). This seems plausible, as this approach neglects the spectral content of the FST and all intricacies of receptivity (Morkovin 1969; Saric et al. 2002). Whereas fundamental research on receptivity is usually studied on a flat plate (Kendall 1997), the situation is particularly complex when applied on boundary layers with pressure gradients, as on NFL-airfoils (Bertolotti 2001).

Therefore, efforts are made to establish flow conditions in the Laminar Wind Tunnel (LWT) of the Institute of Aerodynamics and Gas Dynamics at the University of Stuttgart (Wortmann and Althaus 1964) that are comparable to real FST. This will enable to test airfoils, as well as to conduct fundamental transition research, both under operational conditions of small aircraft and wind turbines. For this purpose, this study aims to characterise natural FST in the convective boundary layer with special account to sailplane operation.

The principal parameter of FST is the intensity of the turbulence, which is related to the dissipation rate of turbulent kinetic energy ε. However, the laminar-turbulent transition is

also sensitive to parameters such as the spectral distribution of the turbulent energy as well as the degree of isotropy and homogeneity (Boiko et al. 2002).

The spectra and the dissipation rate ε are inherently linked to the concept of the Richardson–Kolmogorov energy cascade (Richardson 1922; Kolmogorov 1941). Turbulent energy is generated at large scales and passed on through the inertial range of the spectrum down to the smallest scales, where it is dissipated. As long as these ranges are clearly separated, and under equilibrium conditions, the dissipation rate ε is nearly equal to the rate at which turbulent energy is created and reached down (Pope 2000). This makes the dissipation rate ε a suitable measure for the intensity of turbulence. For homogeneous turbulence, Kolmogorov's considerations lead to the $-5/3$ exponential law of the spectrum of turbulent energy $E(\kappa)$ in the inertial range (Pope 2000):

$$E(\kappa) = C\varepsilon^{2/3}\kappa^{-5/3} \tag{1}$$

which is a function of the wavenumber κ and involves the Kolmogorov constant C.

In case of sailplane application, the convective atmospheric boundary layer is relevant, as most cross-country flights of sailplanes make use of thermals. The altitude range in which sailplanes fly is the convective mixed layer, which extends from the basis of the capping inversion z_{inv}, down to $0.1\, z_{inv}$ (Kaimal and Finnigan 1994).

Dissipation rates have been measured as early as in the 1930ies with respect to gusts on transport airplanes using flow vanes (Küssner 1932; Rhyne and Steiner 1964; MacPherson and Isaac 1977; Sharman 2016).

In-flight measurements with hotwire constant temperature anemometers (CTA) are capable of measuring smaller scales. MacCready (1962) and Zanin (1985) provided measurements of ε and turbulence intensities Tu, respectively, from flights with sailplanes in or close to different sources of updraft. Arntz (1991), Weismüller (2011), Reeh (2014) and Guissart et al. (2021) used light airplanes to make measurements in different conditions of light to moderate turbulence. Wildmann et al. (2021) equipped a powered sailplane to measure wind and dissipation rates ε on lee wave flights in the Andes with a five-hole probe.

A review of further in-flight test campaigns under a wide range of conditions can be found in Arnal (1992) and Riedel and Sitzmann (1998). However, the present study focuses on the convective mixed layer.

Although the correlation between the dissipation rate and terms like "moderate turbulence" is not exactly consistent between the authors, there is a range of ε from 10^{-5} to 10^{-2} m^2/s^3 for the convective atmosphere, and ε from 10^{-6} to 10^{-7} m^2/s^3 for the stable atmosphere.

More recent in-flight measurements (Reeh 2014; Guissart et al. 2021) provide a direct insight into smaller scales (up to 4 kHz) which are more relevant for airfoil boundary layers, and which show the beginning of the dissipation range. Recently, longitudinal velocity fluctuations u' and inflow angle fluctuations α' have also been analysed and provide relations between the standard deviation of the fluctuations and ε (Weismüller 2011; Guissart et al. 2021).

For the design, assessment and optimisation of NLF-airfoils, the better characterisation of atmospheric FST turbulence must be complemented with the information about the level of turbulence during the intended operational profiles. For example, for sailplanes there is little information about the intensity and variance of turbulence in and between thermals, and the dependence on, e.g. the thermal strength. For this purpose, longer data recordings from cross-country flights are obtained in the present investigation.

Guissart et al. (2021) have demonstrated how different the airfoil boundary layer can evolve in free flight and wind tunnel despite the same parameters (Re, ε, wing chord). A broad data basis seems appropriate first to investigate the differences of the FST in flight and in the wind tunnel, and second to develop more realistic simulation techniques.

In this study, a modern high-performance sailplane was equipped with an x-wire CTA, and FST was measured during cross-country flights on several days. The paper covers a total of 22 h of in-flight measurements and their detailed analysis for the design of wind tunnel experiments and numerical studies.

2 Experimental set-up

2.1 Installation

Providing ample space and performance, a two-seat sailplane with 20 m wingspan (Schempp-Hirth Arcus) carried the measuring equipment. The Dantec 55P61 x-wires (1.25 mm long, modified to 2.5 μm diameter tungsten wire) are mounted on a 1.3 m long boom, extending from the left wing nose at a spanwise position of $y = 2.0$ m relative to the plane of symmetry (Fig. 1), close to the nodes

Fig. 1 Boom with (**1**) x-wires, (**2**) accelerometers and (**3**) Prandtl-tube attached to sailplane wing nose

of the various eigenmodes of the airframe. The boom also houses the CTA bridges and amplifiers, whereas the data logger and the power supply are placed inside the fuselage.

The CTA-circuits are custom-built to combine low-noise and small size (Baumann 2013). Based on a standard square wave test, the upper frequency limit of the CTA system is in the order of 10 kHz. The signals are stored direct coupled (DC) as well as AC-coupled with a cut-off frequency $f_c = 0.5$ Hz and amplified by a factor of 300 (AMI 351A-3-50-NI amplifiers). Because of the inherent electronic f^2-noise of CTAs at high frequencies (Freymuth and Fingerson 1997), a 24-bit $\Delta\Sigma$ A/D converter (Bourdopoulos et al. 2003) DT9837B and a high sampling rate of $f_{SR} = 105$ kHz are used. Aliasing is suppressed by the $\Delta\Sigma$-filter with $f_c = 0.49\, f_{SR}$ and an analog low-pass filter with $f_c = 0.4$ MHz. The signal to noise ratio of the converter and the exploitation of the metering range results in an effective number of bits of 14.

Environmental data are collected at a sampling rate of $f_{SR} = 189$ Hz for correcting the CTA readings and calculating pressure altitude and air density. Sensors for dynamic pressure (First Sensor HCLA0025EU) and static atmospheric pressure (First Sensor HDI0611AR) were connected to a Prandtl-probe above the fuselage tailcone. From the third flight on, an additional probe was attached to the boom to provide the dynamic pressure and to obtain a correction for the fuselage influence on the pressure readings. Temperature was measured with a miniature NTC resistor (B + B sensors TS-NTC-833) and relative humidity with a capacitive sensor (Honeywell HIH-4000–004). The related time constants (1/e) range between < 5 ms for the dynamic pressure system to 5 s for the humidity sensor.

A 3-axis accelerometer (NXP FXLN8372Q) was attached 9 cm behind the x-wire to detect vibrations of the boom tip. Measurement procedures were run on a Pico-ITX form factor PC, the capacities of the battery and the solid state hard disc allowed recordings of up to nine hours.

The longitudinal and transversal velocities u and v and their fluctuations (denoted by primes) are processed relative to the probe axis (Fig. 2). The reference for the longitudinal direction, i.e. the x-direction, is the direction of inflow. Owing to the changes in the angle of attack of the aircraft, the probe swivels around the low-pass-filtered inflow-direction through angles in the order of $\Delta\alpha = \pm 4°$.

The nonstationary mean inflow speed is expressed by U_{TAS} calculated from the dynamic pressure, and by U_{CTA}
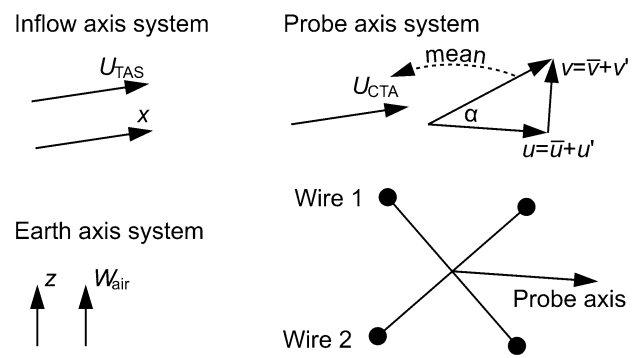

Fig. 2 Reference systems

calculated from the CTA signals. The earth axis system is used for altitudes z within the atmospheric boundary layer as well as for the vertical velocity of the air W_{air} and sailplane sink rates.

2.2 Hotwire calibration

The CTA bridges and wires were pre-calibrated once in the LWT. During the essential part of the recorded cross-country flights, the ambient temperature T varied between 5 and 20 °C, and air densities ρ between 0.9 and 1.1 kg/m³. The pre-calibration did not allow to vary temperature and density within this range.

Different approaches are published to address the effect of the large temperature changes on the CTA output. Here, an approach by Miley and Horstmann (1991) is used capable to regard for temperature and density effects:

$$A + \frac{BE^2}{K_f(T_w - T)} = \left(\frac{V_e d_w}{\nu_f}\right)^{n_1}\left(\frac{\varrho}{\varrho_0}\right)^{n_2} \tag{2}$$

with the CTA output voltage E, the velocity normal to the wire V_e, the fluid thermal conductivity K, the wire diameter d_w, the kinematic viscosity ν and the air density during pre-calibration ρ_0. The index f denotes film conditions, defined by the average of the wire temperature T_w and T. The parameters A, B, n_1, n_2 are calibration constants. The thermal conductivity can be calculated according to Kannuluik and Carman (1951), and ν from the Sutherland formula and from ρ. Hultmark and Smits (2010) showed that the physical terms in Eq. 2 are qualified to represent the influence of even large temperature changes.

The calculation of u and v from the wire normal velocities follows the effective angle method, see Bruun (1995), applying a cosine yaw function. Several hours of operation

after the pre-calibration, the necessity for further correction becomes evident on both, the drift of the measured inflow angle $\alpha = \arctan(v/u)$, and on the drift of the ratio of the measured, one-dimensional velocity spectra E_{11}/E_{22}, where index 1 applies to the longitudinal direction and index 2 to the transversal direction. The straightforward approach to calibrate A, B, n_1, n_2, T_w for each wire from U_{TAS} requires the independent measurement of α to obtain each wire normal velocity. However, an independent measurement of α was not implemented.

With the assumption that Eq. 2 is able to predict the influence of temperature and air density correctly, the remaining degree of freedom is the effective T_w, which could drift through ageing of the wires or other influences upon the CTA closed control loop. As only the temperature difference $\Delta T = (T_w - T)$ enters the equation, and not the absolute wire temperature, the parameters A, B, n_1, n_2 for a given ΔT should not be affected by a varying T_w, as long as the physical properties K_f and v_f are determined correctly for $T_f = T_w - \frac{1}{2}\Delta T$. Therefore, A, B, n_1 for each wire are kept constant at the value of the pre-calibration.

Independent in-flight determination of the density exponent n_2 is not feasible, due to the strong coupling of ρ and T in the atmosphere, which leads to an ill-conditioned transformation of Eq. 2. Therefore, a value of $n_2 = 0.25$ was used, as described in Miley and Horstmann (1991).

The initial wire temperatures during pre-calibration are estimated as $T_{w,1} = 181$ °C and $T_{w,2} = 151$ °C, based on the wire cold resistances and the fixed hot resistance of 20 Ω of the CTAs. To identify the best-to-assume value of T_w for a part of a flight and for each wire, the flight data is processed with different deviations from the initial T_w. The values are chosen according to the following criteria:

Inflow speed: $U_{CTA} = \sqrt{u^2 + v^2}$ should match U_{TAS}.

Isotropy: Due to the assumption of isotropy at small scales, $\partial u'/\partial x$ and $\partial v'/\partial x$ should not correlate.

The spatial derivatives $\partial/\partial x$ are calculated by applying the Taylor hypothesis (see Sect. 2.3):

$$\partial/\partial x = -(\partial/\partial t)/U_{TAS}$$

The inflow speed criterion, i.e. the minimum of the root mean square (RMS) of $((U_{CTA} - U_{TAS})/U_{TAS})$, and the isotropy-criterion, i.e. $\overline{(\partial u'/\partial x)(\partial v'/\partial x)} = 0$, result in perpendicular curves in the $T_{w,1}$, $T_{w,2}$-plane, which allow an unambiguous choice of the $T_{w,1}$, $T_{w,2}$-values (Fig. 3). This process is repeated for every third of each flight. Assuming that the wire temperatures are a function of time, they can be fitted with a polynomial of degree 2. The trend within the flights fits well to the trend over all
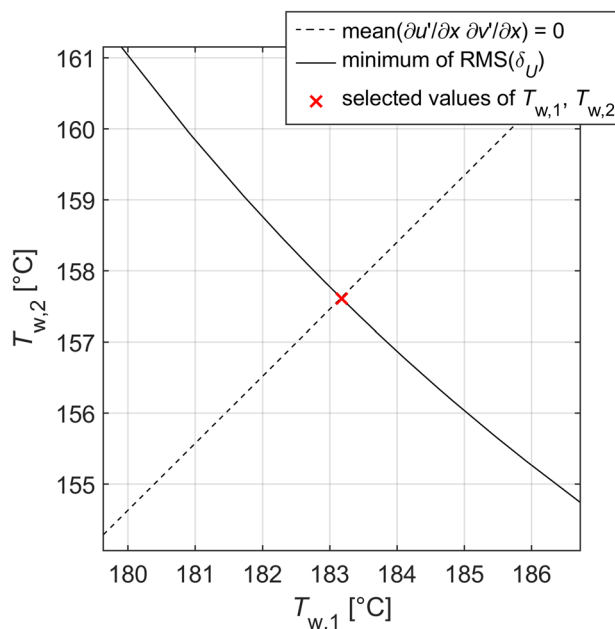

Fig. 3 Determination of effective wire temperatures $T_{w,1}$ and $T_{w,2}$ during flight from the curve of minimum error of the inflow speed $\delta_U = (U_{CTA} - U_{TAS})/U_{TAS}$ and from the condition for non-correlation of $\partial u'/\partial x$ and $\partial v'/\partial x$. Data for the central third of flight 1
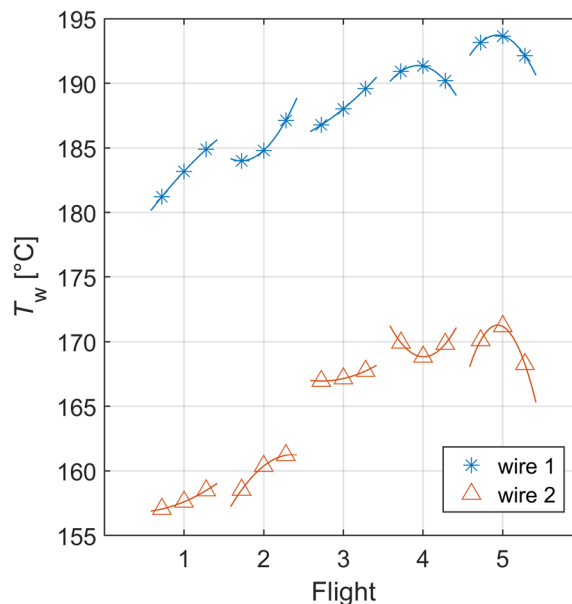

Fig. 4 Effective wire temperatures $T_{w,1}$ and $T_{w,2}$ for flights 1–5 in chronological order. Values were determined for the first, central and last third of each flight, fitted with a polynomial of degree 2
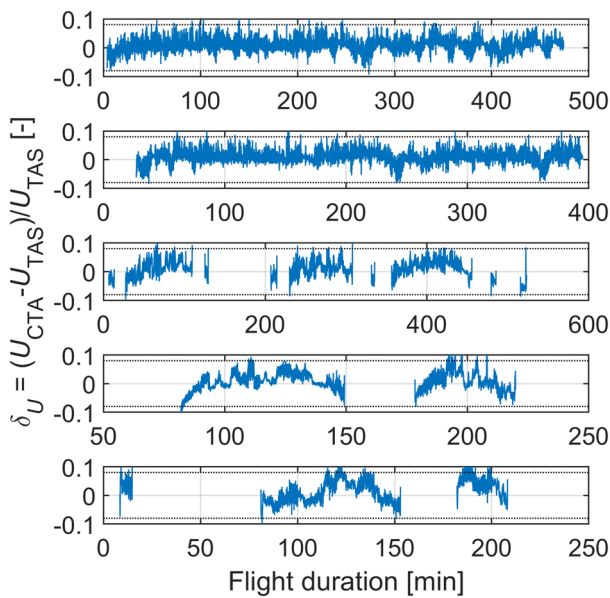
Fig. 5 Relative error of calibrated U_{CTA} compared to U_{TAS} from the Prandtl-probe versus flight time. Dotted lines at $\pm 8\%$ for comparison. From top to bottom: flight 1 to 5

flights (Fig. 4). The resulting relative error of the CTA inflow speed $\delta_U = (U_{\text{CTA}} - U_{\text{TAS}})/U_{\text{TAS}}$ for the five flights is plotted in Fig. 5, together with lines for $\pm 8\%$. The RMS value of δ_U remains between 2,0 and 3,9% for the different flights. It follows from Eq. 1 that the relative error δ_ε of the dissipation rate ε relates as $(1 + \delta_\varepsilon) = (1 + \delta_U)^3$, and therefore reaches peak values as large as 33%, but based on RMS(δ_U) = 3.9% it results in 12%.

Of course, the processed data can no longer be used to evaluate the correlation of $\partial u'/\partial x$ and $\partial v'/\partial x$, because the non-correlation was used as a precondition.

2.3 Postprocessing

In cross-country flights, in contrast to previous studies (Weismüller 2011; Reeh 2014; Guissart et al. 2021), steady-state flight conditions are not maintained. To achieve a necessary degree of stationarity, the flights are divided into subsegments of 4 s. This time step is long enough for the evaluation of spectra and short enough to keep the changes in the flight and environmental conditions small. Calculation of the u and v velocities are based on Eq. 2, where the electric signal E of the CTA is composed of the AC-coupled signal and a linear fit of the direct coupled signal. The AC-coupled signal is corrected by a Fourier and inverse Fourier transform procedure for amplification and phase shift of the amplifiers down to 0.8 Hz. Power spectral densities (PSD) are calculated for

each subsegment with the Welch algorithm (Bendat and Piersol 2010) on 50 blocks of 2^{14} samples of the AC-signal with a Hann-window and 50% overlap. For frequencies below 6 Hz, the DC-signals are processed similarly with 5 blocks of 2^{17} samples. In general, the spectra from the AC-signals show a better signal to noise ratio (SNR) in the dissipation range. The frequency $f_{\text{onset noise}}$, above which the SNR falls below 7 dB due to the CTA f^2-noise, ranges from 0.9 to 6.8 kHz depending on the turbulence level. For spectra of $\kappa < 0.44$ rad/m, the direct coupled CTA and environmental data are low-pass-filtered and downsampled to 94.5 Hz.

Wavenumbers are calculated using the Taylor hypothesis of frozen turbulence $x = -U_{\text{TAS}} t$, leading to $\kappa = 2\pi f/U_{\text{TAS}}$. The use of the Taylor hypothesis is justified, first because the velocity fluctuations are small compared to the mean velocity (Nobach and Tropea 2012), i.e. the flying speed of the sailplane, which typically ranges between 25 and 35 m/s (thermalling phases) and 28–50 m/s (straight legs). Second, there is no preferential convection velocity in the longitudinal direction, which fulfils the criterion of Romano et al. (2007). However, limitations are discussed in Sect. 3.1.

The spatial resolution of the x-wires has an effect on the frequency response of the CTA system. A correction according to Zhu and Antonia (1996) is applied, but has only an effect of 3–5% at a wavenumber of 700 rad/m, as well as it has only a negligible effect on the probability densities distributions (PDF) of $\partial u'/\partial t$ and $\partial v'/\partial t$.

During some periods of time, the CTA signals display up to 20 peaks per metre along the flight path, each peak on a single x-wire channel only and one or two samples wide. These peaks probably stem from impact of pollen on the wires. Affected subsegments are excluded from estimating the probability density functions because a single peak can increase the kurtosis by an order of magnitude. For the calculation of spectra, up to three peaks per second are tolerated.

Adopting the method of Djenidi and Antonia (2012), the dissipation rate ε is determined by least squares fitting the Pope model spectrum of E_{11} (Pope 2000) to the inertial and dissipation range of the measured spectrum. The model spectrum is defined as:

$$E(\kappa) = C\varepsilon^{2/3}\kappa^{-5/3}f_L(\kappa L)f_\eta(\kappa \eta) \tag{3}$$

where $C = 1.5$ is used, and $f_L(kL)$ and $f_\eta(k\eta)$ are non-dimensional functions, determining the shape of the energy-containing range and the dissipation range, respectively. The Kolmogorov lengthscale η calculates as:

$$\eta = \left(\nu^3/\varepsilon\right)^{1/4}. \tag{4}$$

Table 1 Cross-country flights used for this study

Flight Nr.	Date, Time of first and last record relative to solar noon [h:min]	Duration w/o take-off and landing [h:min]	Mean vertical air velocities during thermalling phases [m/s] (mean ± std)	Relative humidity indicated in flight [%] (14–86% percentile)	Mean wind speed in thermalling phases [m/s] (14–86% percentile)	QNH [hPa]
1	3 June 2018 −2:45 to 5:06	7:44	2.7 ± 1.5	5–20	1–5	1016
2	4 June 2018 −2:45 to 3:23	5:57	2.7 ± 1.6	0–15	1–6	1012
3	15 Aug. 2018 −2:30 to 3:23	4:30	2.2 ± 1.5	70–90	3–5	1020
4	17 Aug. 2018 1:00 to 3:18	1:48	3.3 ± 1.6	50–65	2–6	1015
5	16 Sept. 2018 −0:59 to 2:20	1:44	1.4 ± 1.3	5–10	2–4	1023

Flight Nr.	Convection condensation level from sounding, above MSL [m]	Showalter index [-] Lifted Index [°C] CAPE [J/kg]	Clouds	Remarks
1	1550	−0.87 −2.58 °C 760 J/kg	Cu scattered—broken, Cs, Ci fields	Small scale high-pressure ridge; cold high-altitude air destabilising from South-West
2	2100	−1.44 −2.54 °C 545 J/kg	Cu few-scattered	Transition to flat low-pressure situation, weak stable stratification at 700–750 hPa
3	1400	2.96 3.43 °C 17.5 J/kg	Cu broken, in cyclic alternation with cloud screening	On the back of a cold front; a wedge of the Azores high coming in; strong inversion at 2600 m
4	2500	−1.17 −2.91 °C 400 J/kg	Cu scattered, broken, overdevelopment and showers	Weak through of low pressure; becoming more unstable with an approaching cold front
5	3300	15.0 8.37 °C 0 J/kg	no Cu, thin Cs	A high in Central Europe; low-pressure gradients; rough thermals

The longitudinal E_{11} and transverse E_{22} spectra are derived as:

$$E_{11}(\kappa_1) = \iint_{\kappa_1}^{\infty} \frac{E(\kappa)}{\kappa}\left(1 - \frac{\kappa_1^2}{\kappa^2}\right)d\kappa$$

$$E_{22}(\kappa_1) = \frac{1}{2}\left(E_{11}(\kappa_1) - \kappa_1 \frac{dE_{11}(\kappa_1)}{d\kappa_1}\right).$$

When possible, the subsegments are assigned to flight phases (Maughmer et al. 2017), based on the GPS-flight log. In particular, these phases are thermalling and straight legs. Basic criterion for thermalling phases is a minimum average rate of turn of 0.05 rad/s. Only thermalling phases with more than three turns are regarded and transients during entering and exiting are removed. Straight legs continue as long as the flight path does not deviate from the general direction of this phase by more than 45°, and they have to last at least 60 s.

The vertical air velocity W_{air} is calculated from the rate of change of the total energy E_{total} and the polar sink rate w_{pol} of the sailplane:

$$W_{air} = \frac{dE_{total}}{dt}/g + w_{pol}$$

where $E_{total} = Hg + 0.5\, U_{TAS}^2$, with g as the gravitational acceleration and H as the pressure altitude. In thermalling phases, the average circling radius R and the flying speed are taken into account for the polar sink rate in turns:

$$c_{\mathrm{L}} = \sqrt{\left(U_{\mathrm{TAS}}^2/R\right)^2 + g^2} \, m / \left(\frac{1}{2} U_{\mathrm{TAS}}^2 \rho S\right)$$

$$w_{\mathrm{pol}} = U_{\mathrm{TAS}} c_{\mathrm{D}}(c_{\mathrm{L}}) \left(\frac{1}{2} U_{\mathrm{TAS}}^2 \rho S\right) / (mg)$$

where S is the wing area, m is the sailplane mass, and $c_{\mathrm{D}}(c_{\mathrm{L}})$ is the drag coefficient of the sailplane.

Of course, $c_{\mathrm{D}}(c_{\mathrm{L}})$ is associated with some uncertainty. As no flap settings were recorded, only an envelope polar can be used, and the drag of the installation can only be estimated, with $\Delta c_{\mathrm{D}} S = 0.015 \text{ m}^2$. The use of the total energy E_{total} accounts for the altitude gain in pull-ups and vice versa. W_{air} shows some scatter (see Figs. 12, 16), especially in turbulent air. This approach is unable to resolve dynamic situations as it assumes that the sailplane adapts its own climb rate to the changing W_{air} instantly. Systems designed specifically for wind measurements in flight are described in Pätzold (2018) and Wildmann et al. (2021).

2.4 Flights and meteorological conditions

Flights were conducted in southern Germany along the Swabian Alps from May to September 2018. The data of five flights were considered analysable, involving 22 h of recorded flight time (Table 1). Flights 3–5 are composites of more flights on that day (see Fig. 5), but nevertheless are referred to as a "flight". General meteorological conditions ranged from low-pressure to high-pressure conditions. Days with normal smooth thermals are included as well as a day, on which thermals were experienced by the pilot as exceptional rough (flight 5). The flights were conducted in pressure altitudes between 1000 and 2500 m. Atmospheric data given in Table 1 are based on ground and altitude weather maps, and radio soundings (Oolman 2021) from the Stuttgart airport (WMO station 10,739), which is located about 60 km west and about 330 m lower than the airfield. The classification of clouds is based on notes, the meteorological data, and on a single snapshot in form of an afternoon satellite image.

3 Results

This study aims at the description of the FST during thermalling and on straight legs during soaring cross-country flights. Characteristic lengthscales and the possibilities of obtaining them from the data are discussed in Sect. 3.1. Statistic quantities of $\partial u'/\partial x$ and $\partial v'/\partial x$ including skewness and kurtosis as a measure of quality control are discussed in Sect. 3.2. The FST structure, mainly with respect to the obtained dissipation rates, is discussed in Sect. 3.3 for the typical thermalling phase, in Sect. 3.4 for the typical straight leg, and in Sect. 3.5 averaged over the whole flights.

3.1 Characteristic lengthscales

To describe the dimensions of turbulent spectra, lengthscales are used (Pope 2000). A measure for the energy-containing structures is the integral lengthscale Λ_i (Romano et al. 2007):

$$\Lambda_i = \int_0^\infty R_{ii}(x) \mathrm{d}x$$

where $R_{11}(x)$ and $R_{22}(x)$ are the autocorrelation of u' and v', respectively. A measure for the intermediate scales between energy-containing range and dissipation range is given by the Taylor microscale λ_i, which is the distance at which a parabolic approximation of the autocorrelation $R_{ii}(x)$ vanishes (Romano et al. 2007).

However, for two reasons the in-flight measurements of this study do not qualify for the determination of either lengthscale. First, measurements are not made under stationary conditions. Control inputs and the sailplane longitudinal stability cause pitch and speed changes, and on the large scale the transversal flow at the boom is defined by the polar sink rate. Therefore, neither the large-scale turbulent fluctuations u' and v' can be isolated, nor can the onset of the energy-containing range in the atmospheric spectra be determined. To overcome this problem, the proper motion of the sailplane must be determined, as described, e.g. in Pätzold (2018) or Wildmann et al. (2021). Second, the probe is not traversed in a straight line through the atmosphere, which corrupts the Taylor hypothesis of frozen turbulence on the large scale, and, as the probe returns to similar areas during thermalling, an artificial correlation is introduced.

In measurements that are not compromised by these difficulties, the size of the eddies with the most energy can be estimated from the wavelength $\Lambda_{\mathrm{m},i}$ at which $\kappa_i E_{ii}$ peaks (Kaimal and Finnigan 1994). In the convective mixed layer and in the altitude band predominantly used for soaring, $\Lambda_{\mathrm{m},i}$ is approximated with 1.5 z_{inv} in horizontal direction and z_{inv} to 1.6 z_{inv} in the vertical direction (Caughey and Palmer 1979). With $\Lambda_1 \approx 1/\kappa_{\mathrm{m},1} = \Lambda_{\mathrm{m},1}/(2\pi)$ (Kaimal and Finnigan 1994), the longitudinal integral lengthscale can be estimated as $\Lambda_1 \approx 1.5 \, z_{\mathrm{inv}} / (2\pi) \approx 0.2 \, z_{\mathrm{inv}}$. Because cross-country soaring flights only take place with z_{inv} of several hundred metres, Λ_1 can be expected to be of a magnitude of few hundred metres.

This also justifies the assumption of local isotropy at scales relevant for airfoil boundary layer transition—in case of sailplane this corresponds to $\kappa \geq 50$ rad/m, or wavelengths ≤ 0.1 m. In comparison, Pope (2000) takes roughly
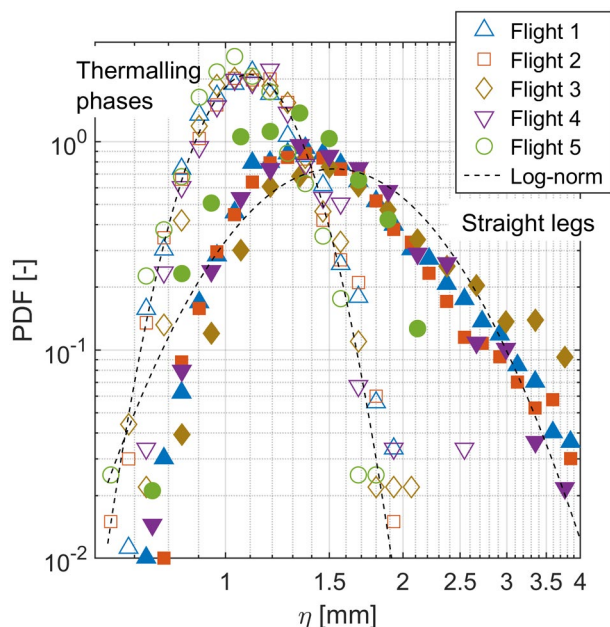
Fig. 6 PDFs of the Kolmogorov lengthscale η for thermalling phases (open symbols) and straight legs (full symbols). Log-normal distribution (dashed lines) based on mean and standard deviation of all flights
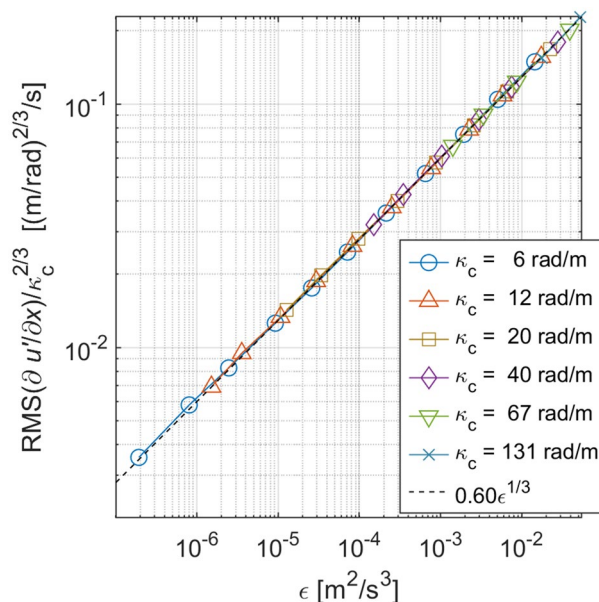

Fig. 7 Velocity derivative $\partial u'/\partial x$ divided by the low-pass cut-off wavenumber $\kappa_c^{2/3}$. Values and ε ensemble averaged over ε-bins. Limited to inertial range with $\kappa_c\eta < 0.1$

$1/6\,\Lambda_1$ as a demarcation between anisotropic large eddies and the isotropic small eddies.

The remaining scale is the Kolmogorov lengthscale (Eq. 4), a measure for the scales of the dissipation range. Figure 6 shows the PDFs of η for thermalling phases and straight legs for each flight. The distributions for thermalling phases are close to log-normal, whereas those for straight legs show considerable scatter, deviating both from the log-normal distribution and from each other flight. The distribution of η is determined by ε because during the flights the kinematic viscosity ν varies only by a factor of 1.2, whereas ε varies by a factor of $2\cdot10^6$. Why thermalling phases and straight legs show different PDFs of ε, and thus of η, is discussed in Sect. 3.3 and 3.4.

3.2 Statistic quantities of $\partial u'/\partial x$ and $\partial v'/\partial x$

Statistics of velocity derivatives $\partial u'/\partial x \approx \left(u'(x+\Delta x,t) - u'(x,t)\right)/\Delta x$ (correspondingly for v; the time argument is omitted in the following) can provide information on the structure of the turbulence in the inertial and dissipation range, which the spectra cannot. For example, the scale-dependent intermittency at small scales and high turbulent Reynolds numbers (Kraichnan 1974), which is indicated by the pronounced tails and increased kurtosis K_u of the PDF of $\partial u'/\partial x$, is evidence that dissipative eddies are not uniformly distributed in space (Tennekes 1968). The skewness S_u of the same PDFs represents the rate of production of vorticity through extension of the vortex lines. (Taylor 1938; Batchelor and Townsend 1947).

The velocities u', v' are processed separately for each sub-segment, using its η and average U_{TAS}. They are low-pass-filtered at different cut-off normalised wavenumbers $(\kappa\eta)_c$ to probe the signals at different scales from the inertial range to the dissipation range. Filtering is done by eliminating the corresponding Fourier coefficients above $f_c = (\kappa\eta)_c\,U_{\text{TAS}}/(2\pi\eta)$. The derivatives are calculated from central differences, and then are downsampled to a sampling rate of $f_{\text{SR}} > 2f_c$ to remove redundant information. The derivatives are separated into bins of different turbulence levels based on η. Only for Fig. 7, the data are filtered at cut-off wavenumbers κ_c and categorised into bins of ε, with two bins per decade. No differentiation by flight phase is made.

According to Kolmogorov (1962), the RMS of the u' difference over a distance r, i.e. $\sqrt{\overline{\left(u'(x+r) - u'(x)\right)^2}}$, scales with $\overline{\varepsilon(x)^{1/3}}r^{1/3}$ in the inertial range for isotropic turbulence, which, e.g. Guissart et al. (2021) demonstrated for their data. As the derivative $\partial u'/\partial x \approx \left(u'(x+r) - u'(x)\right)/r$ is additionally divided by r, its RMS value must scale with $\varepsilon(x)^{1/3}r^{-2/3}$. In our calculation of the derivative, Δx remains constant, but the low-pass-filtering removes all contributions above $r = 2\pi/\kappa_c$, so that:

$$r \sim \kappa_c^{-1} \tag{5}$$

can be applied. Figure 7 shows $\text{RMS}(\partial u'/\partial x)/\kappa_c^{2/3}$ versus the average ε of the bins, for six different cut-off wavenumbers κ_c. Only those combinations are plotted where

$\kappa_c \, (\nu_{\mathrm{ref}}^3/\varepsilon)^{1/4} < 0.1$, to restrict the curves to the inertial range (with $\nu_{\mathrm{ref}} = 1.7 \cdot 10^{-5}$ m²/s, as a typical value). Because the curves collapse to a single curve proportional to $\varepsilon^{1/3}$, the present data is in agreement with this prediction of the theory.

The calculation of PDFs of the $\partial u'/\partial x$ and $\partial v'/\partial x$ requires long enough recordings under stationary conditions. As flights were cross-country flights, this is not granted. A first measure to address this is the use of spatial derivatives, a second is to create the PDFs separately for different bins of turbulence levels. The third measure is to normalise the derivatives (Reeh 2014) with the nonstationary mean and mean square values, which are estimated from moving averages of 4 s integration time (Bendat and Piersol 2010):

$$\left(\frac{\partial u'}{\partial x} \right)^+ = \left(\frac{\partial u'}{\partial x} - \overline{\left(\frac{\partial u'}{\partial x} \right)} \right) \bigg/ \sqrt{\overline{\left(\frac{\partial u'}{\partial x} \right)^2}}.$$

The corresponding definition applies for $(\partial v'/\partial x)^+$.

The skewness S_u and kurtosis K_u for $(\partial u'/\partial x)^+$ are defined as:

$$S_u = \overline{\left(\frac{\partial u'}{\partial x} \right)^{+3}} \bigg/ \left[\overline{\left(\frac{\partial u'}{\partial x} \right)^{+2}} \right]^{3/2}$$

$$K_u = \overline{\left(\frac{\partial u'}{\partial x} \right)^{+4}} \bigg/ \left[\overline{\left(\frac{\partial u'}{\partial x} \right)^{+2}} \right]^{2}.$$

The S_v and K_v for $(\partial v'/\partial x)^+$ are defined accordingly.

Burattini et al. (2008) have investigated the influence of the spatial and temporal resolution of the hotwire on the measurement of the skewness. Wire length and distance between wires are smaller than 2η in the present study. In this case, according to Burattini et al. (2008), the normalised distance between two measuring points $m^+ = U_{\mathrm{TAS}} / (f_{\mathrm{SR}} \, \eta)$ is more relevant. The sampling rate f_{SR} is much higher than $f_{\mathrm{onset\ noise}}$, therefore, an effective $f_{\mathrm{SR,eff}} = 2 f_{\mathrm{onset\ noise}}$ is applied. The limit $f_{\mathrm{onset\ noise}}$ depends on the turbulence level, however, on the $(\kappa\eta)$-scale this limit turns out to be located at $\overline{(\kappa\eta)}_{\mathrm{onset\ noise}} = 0.7$ with a standard deviation of 0.12. This results in $m^+ = \pi / (\kappa\eta)_{\mathrm{onset\ noise}} \approx 4$. According to Burattini et al. (2008), this leads to values of S_u too low by a factor of 0.8. As the differentiation is done after the low-pass-filtering, but with the original sampling rate, there is no effect of the filter cut-off frequency on the discretisation error during differentiation. Filtering only removes the influence of the smaller scales.

Spectra, skewness and kurtosis were calculated for each suitable subsegment. Only such η-bins were used in the following that contain contributions of at least 500 of such subsegments.
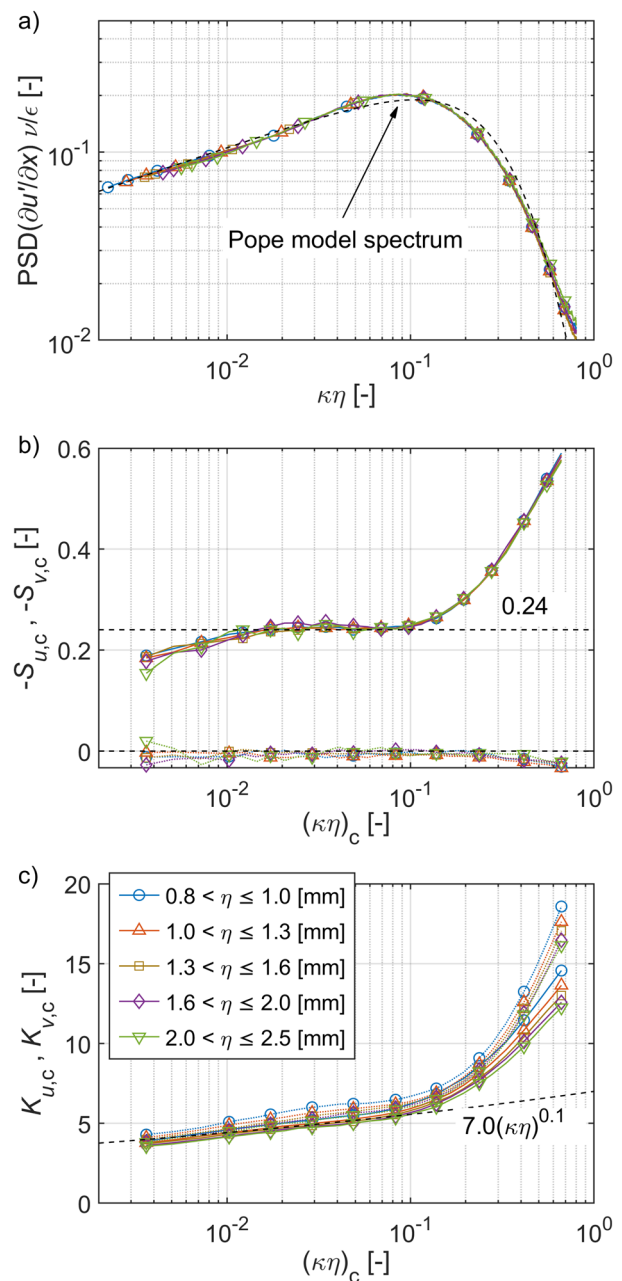
Fig. 8 Statistic quantities of velocity derivatives covering all flights, averaged for bins of different η as a measure for different levels of turbulence. **a** Spectra of $\partial u'/\partial x$ compared to $\kappa^2 E_{11}$ of the Pope model spectrum, both normalised. **b** Skewness and **c** kurtosis of $\partial u'/\partial x$ (solid line) and $\partial v'/\partial x$ (dotted line), both low-pass-filtered for different cut-off normalised wavenumbers $(\kappa\eta)_c$

Figure 8 shows the influence of the cut-off normalised wavenumber $(\kappa\eta)_c$ on skewness $S_{u,c}$, $S_{v,c}$ and kurtosis $K_{u,c}$, $K_{v,c}$ (index c when based on low-pass-filtered data). To illustrate the part of the spectrum that has been cut-off, a plot of the dissipation spectra, i.e. the spectra of $\partial u'/\partial x$, versus $\kappa\eta$ is added (Fig. 8a). The spectra (solid lines with markers) are binned

and averaged for different η, but due to the $\kappa\eta$-scaling and the normalisation with ν/ε, the spectra of all η-bins collapse.

The electronic noise of the CTA gradually sets in above $(\kappa\eta)_c = 0.66$, however, the slope of the spectra can be estimated up to $(\kappa\eta)_c = 0.8$ by subtracting a f^2-fit of the noise in the spectrum of each subsegment. The dashed curve shows the dissipation spectrum of the Pope model spectrum (Pope 2000), calculated as $\kappa^2 E_{11}(\kappa) \nu/(\varepsilon\eta)$. In the dissipation range, the in-flight spectra show a deficit of up to 9% in amplitude compared with the model spectrum, the reason for which could not yet be determined.

Figure 8(b) shows the skewness $S_{u,c}$ (solid lines) and $S_{v,c}$ (dotted lines). Each symbol represents the average within the corresponding η-bin and within the surrounding range of $(\kappa\eta)_c$. For clarity, not all symbols are plotted. The $S_{v,c}$ are close to zero, which is plausible for symmetry reasons, as in the small scales every directional information is lost, and all transversal directions must be equivalent. Sukoriansky et al. (2018) pointed out that for $(\kappa\eta)_c$ in the inertial range, $S_{u,c}$ must be independent of the cut-off wavenumber, and they determined a value between -0.239 and -0.198 for $S_{u,c}$ for Kolmogorov constants C between 1.5 and 1.7, respectively. The value of 0.24 is shown by a dashed line. Below $(\kappa\eta)_c = 10^{-2}$, $S_{u,c}$ falls off, which according to Sukoriansky et al. (2018) results from the lacking contributions of lower wavenumbers.

In the same way, Fig. 8(c) shows the kurtosis $K_{u,c}$ (solid lines) and $K_{v,c}$ (dotted lines). As Sreenivasan and Antonia (1997) point out, the kurtosis of $\left(u'(x+r) - u'(x)\right)$ over an inertial range distance r has shown in experiments to scale with $r^{-0.1}$. Because of Eq. 5, $K_{u,c} \sim \kappa_c^{0.1}$ can be expected. In Fig. 8c, the dashed line with the slope of $(\kappa\eta)^{0.1}$ is in fact parallel to the curves of $K_{u,c}$ in the inertial range.

In the inertial range, the curves of $K_{u,c}$ for the different η-bins collapse closer, when plotted over the cut-off wavenumber κ_c alone, see Fig. 9a. This indicates that the process that increases the kurtosis, is independent of the turbulence level, but dependent on the dimensional κ. Furthermore, Fig. 9b shows that the change in slope of $K_{u,c}$ at the beginning of the dissipation range is associated with $\kappa\eta^{0.6}$.

Wyngaard and Tennekes (1962) derived relations of S_u and K_u with the Taylor microscale Reynolds number Re_λ. However, with the difficulties in determining a reliable value for λ_1, a correlation with Re_λ cannot be demonstrated with the present data. With Re_λ eliminated, $S_u \sim K_u^{3/8}$ remains. Figure 10 shows $S_{u,c}$ and $K_{u,c}$ for the largest exploitable $(\kappa\eta)_c = 0.66$, each dot representing a subsegment of the flights. Although there is considerable scatter, a linear least square fit in the log–log plane results in an exponent of 0.41, thus only 9% higher than the theoretical value.

The statistic quantities of $\partial u'/\partial x$ and $\partial v'/\partial x$ show excellent agreement with the predictions of the theory throughout the different levels of turbulence. The deviation in the
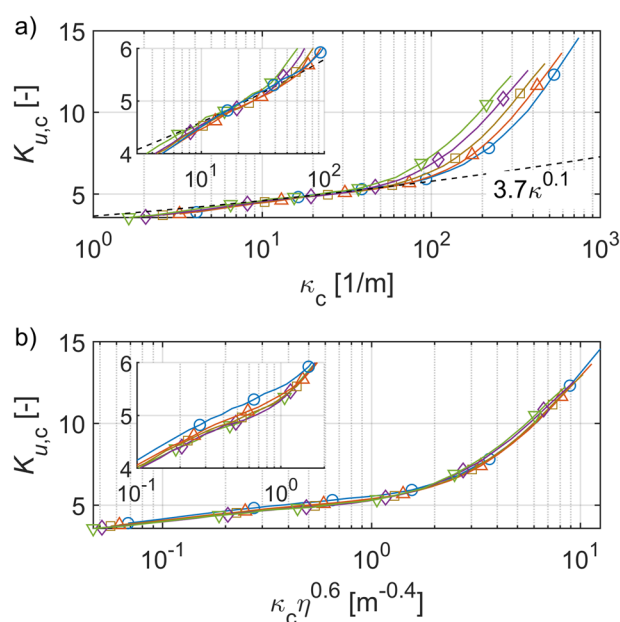

Fig. 9 Kurtosis of $\partial u'/\partial x$ plotted **a** versus the cut-off wavenumber κ_c, matching the curves in the inertial range, **b** versus $\kappa_c \eta^{0.6}$, matching the curves in the transition to the dissipation range. Insets show enlargements. For legend, see Fig. 8
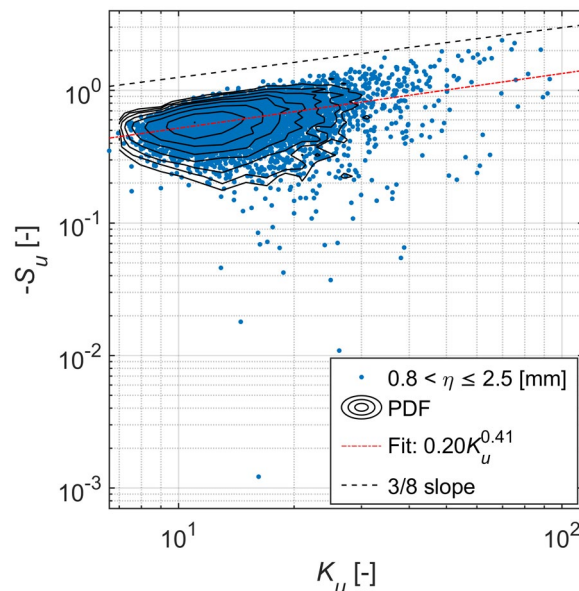

Fig. 10 Relation between skewness S_u and kurtosis K_u at small scales. Each dot represents a 4 s subsegment of the flights, solid lines levels of the joint PDF. Least square fit indicates an exponent of 0.41 compared to $3/8 = 0.375$ from Wyngaard and Tennekes (1962)

dissipation range of the dissipation spectrum remains to be clarified, however, the data are suitable for the analysis of the FST within thermalling phases and between them.

3.3 Thermalling phases

Thermalling phases make up 27% of the flight time, two-third or 99 of these extend over more than three turns, 58% of the flight time is recognised as straight legs, and the remaining 15% are either not classified or are counted as transients.

During thermalling, average flying speed was 31.5 m/s with a standard deviation of 2 m/s. For every thermal, a mean circling radius is determined, which in average over all thermalling phases is 139 m with a standard deviation of 24.5 m.

The thermalling phase with the largest altitude gain of 1500 m is used to present some characteristics (flight 4, thermal 7). Figure 11 shows the flight path, with symbols the size of which represents the magnitude $\varepsilon^* = \log_{10}(\varepsilon/(\mathrm{m^2/s^3}))$ of the dissipation rate and their colour denotes the vertical air velocity W_{air}. The most noticeable feature is the displacement by the wind and the irregularities due to the pilot's attempts to manoeuvre into the direction of the strongest climb. Thus, the pilot to some degree corrupts the statistical independence of successive data points, however under the influence of wind this active control is required not to leave the thermal to the lee side, as the air rises steeper than the sailplane.

The dissipation rate ε and W_{air} do not change significantly with height, but more within single turns. This is shown more clearly in Fig. 12, in which ε and W_{air} are plotted

Fig. 12 Thermal of Fig. 11: ε^* and W_{air} as functions of the angular position within the circles of the flight path

versus the angle φ, from the flight path to the centre of the circles. The correlation of ε^* with the angular position is most prominent around $\varphi = 3600°$. The glider must have circled between areas of different turbulence intensity. It is not possible to demonstrate an equally well correlation between W_{air} and ε, which is due to the significantly larger time constant in the determination of W_{air}.

Figure 13 shows the longitudinal spectra E_{11} and the PDF of ε^*. The spectra of three subsegments represent the 5%, 50% and 95% percentile of the ε-range within this thermalling phase. All spectra are clipped at $f_{\mathrm{onset\ noise}}$. The spectra fit closely to the Pope model spectra.

For more information about the statistical distribution of the dissipation rate, all thermalling phases of each flight are combined. The dissipation rates of the subsegments within the i-th thermal are normalised to make them comparable.

$$\varepsilon^*_{\mathrm{norm}} = (\varepsilon^* - \mu_i)/\sigma_i$$

where μ_i and σ_i are the mean and the standard deviation of ε^* within thermal i. Figure 14 shows the PDFs of $\varepsilon^*_{\mathrm{norm}}$ for all five flights. They agree well with the standard normal distribution, which suggests a log-normal distribution of ε. Table 2 lists the mean values and standard deviations of μ_i and σ_i/μ_i, which allow to model distributions of absolute values of ε.

The log-normal distribution of ε is in agreement with the assumption made by Obukhov (1962) and Kolmogorov (1962) in context with the refined similarity hypotheses

Fig. 11 Thermal with largest altitude gain: Flight path with ε represented by symbol size and W_{air} by colour. GND: above ground level
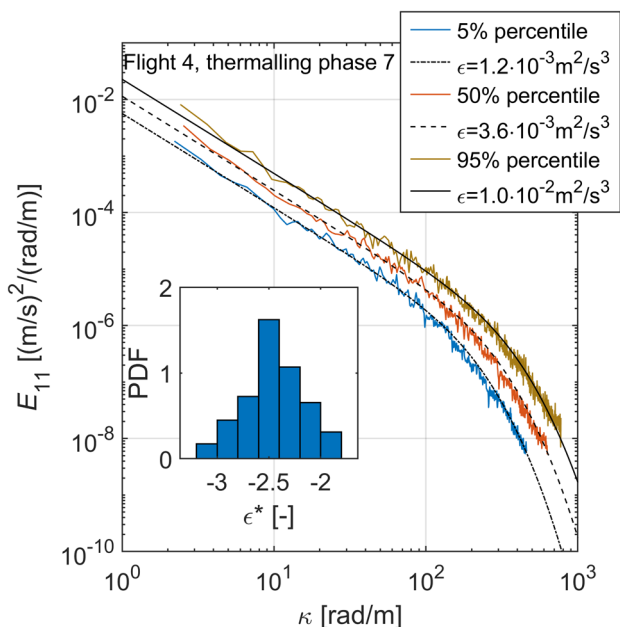
Fig. 13 Thermal of Fig. 11: Longitudinal spectra of 4 s subsegments, the dissipation rates of which represent the 5%, 50% and 95% percentiles in this thermal. Comparison with Pope model spectra (black). Inset: PDF of ε^* recorded in this thermal

Table 2 Statistics of the dissipation rate in thermalling phases of the five flights

Flight	Mean μ_i	Std.dev. μ_i	Mean (σ_i/μ_i)	Std.dev. (σ_i/μ_i)
1	−2.38	0.19	−0.098	0.025
2	−2.45	0.17	−0.096	0.024
3	−2.49	0.16	−0.100	0.030
4	−2.40	0.12	−0.109	0.030
5	−2.42	0.11	−0.100	0.024

Based on the average μ_i and the standard deviation σ_i of ε^* within thermal i, where $\varepsilon^* = \log_{10}(\varepsilon/(m^2/s^3))$ is the magnitude of the dissipation rate

(Pope 2000). They assumed the local dissipation rate ε_r for a small volume of radius r to be log-normally distributed. Obviously, the distance flown within the subsegments (~120 m) is sufficiently small, and despite the fluctuations of ε partially correlate with the angular position in the circles, the turbulence is sufficiently homogeneous along the helical flight path around the thermal core.

3.4 Straight legs

Within the flights, 217 straight legs have been identified. The flying speed averaged 38 m/s with a standard deviation of 5.8 m/s. While thermalling is made exclusively in updrafts, it is less straightforward to associate certain
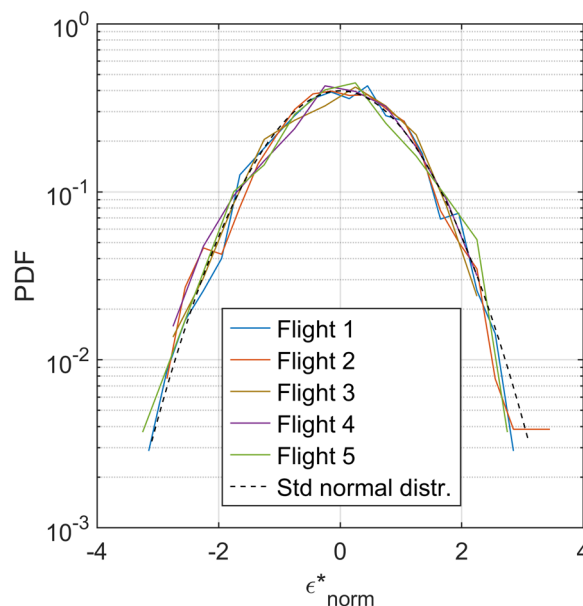
Fig. 14 PDF of $\varepsilon^*_{\text{norm}}$, which is ε^* normalised with the mean and the standard deviation of ε^* within the thermal it was recorded in
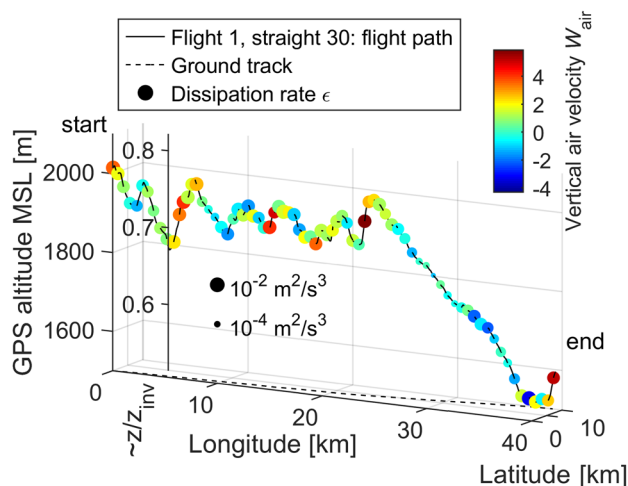
Fig. 15 Straight leg with longest duration: Flight path with ε represented by symbol size and W_{air} by colour. MSL: above sea level

atmospheric conditions with the straight flight between thermals. Although the glider pilot seeks to fly through raising air, the sailplane may also have crossed areas of still air or downdrafts. The straight leg with the longest duration is presented in Figs. 15, 16 and 17. Figure 16 shows that in the first 600 s the pilot is able to maintain his altitude due to an average W_{air} of 0.9 m/s. Between $t=600$ s and 840 s the average W_{air} drops to -0.4 m/s. A change of the mean dissipation rate ε is visible between both periods, from $2.1 \cdot 10^{-3}$ m^2/s^3 ($t=0$–600 s) to $4.6 \cdot 10^{-4}$ m^2/s^3 ($t=600$–840 s), see dashed
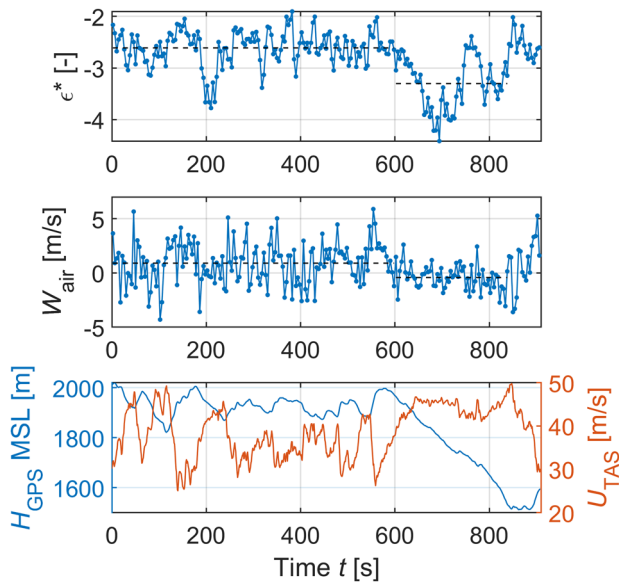
Fig. 16 Straight leg of Fig. 15: ε^*, W_{air}, GPS altitude above sea level H_{GPS} MSL and U_{TAS} plotted versus time t. Dashed lines: mean values for $t = 0$ to 600 s and for $t = 600$ s to 840 s
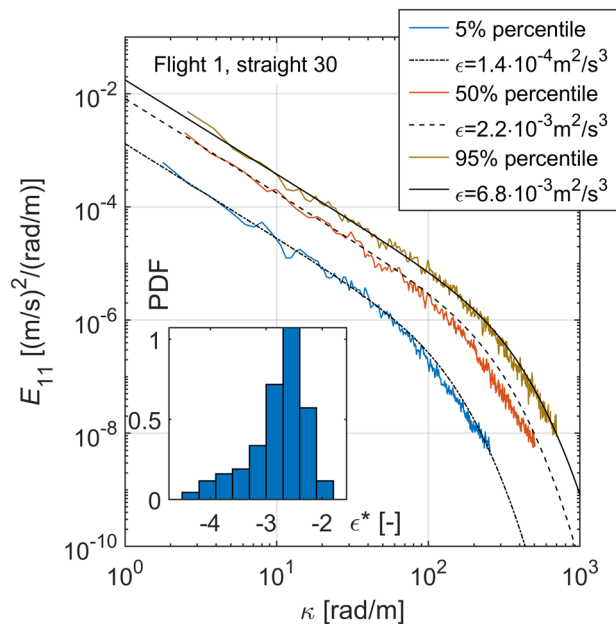

Fig. 17 Straight leg of Fig. 15: Longitudinal spectra of 4 s subsegments, the dissipation rates of which represent the 5%, 50% and 95% percentiles in this straight leg. Comparison with Pope model spectra (black). Inset: PDF of ε^* recorded in this straight leg

lines in Fig. 16. The loss of 400 m of altitude between $t = 600$ s and 840 s not only accounts to the sinking air mass, but also to the acceleration and higher polar sink rate, as the pilot increases the flying speed according to the speed-to-fly theory. The 5%, 50% and 95% percentile spectra show a

good agreement with the Pope model spectrum (Fig. 17), but the PDF of ε^* now deviates clearly from a normal distribution as it is a composite of at least two normal distributions for different mean values.

The flight phases between thermals do not represent uniform atmospheric conditions, and the dissipation rate ε cannot be expected to follow a specific probability distribution.

3.5 Overall spectra and dissipation rates

Figures 18, 19, 20 and 21 show E_{11} and E_{22} averaged over all thermalling phases and straight legs, respectively, of each flight. The flight spectra for $\kappa > 0.44$ rad/m are averaged from the spectra of the subsegments, whereas spectra for $\kappa < 0.44$ rad/m are calculated from downsampled 94.5 Hz data with a blocklength of 2^{14} only for thermalling phases or straight legs of at least 174 s duration. Therefore, the low wavenumber spectra use only a fraction of the flights as data basis. For $\kappa < 0.1$ rad/m, the flight spectra deviate strongly from the $-5/3$ slope. At these wavenumbers, the E_{11}-spectra rise due to variations of the flight speed, while the E_{22}-spectra are attenuated, as the sailplane adopts to the climb or sink rate of long wavelength vertical gusts. The continuing increase in E_{22} towards low wavenumbers in Fig. 21 may be related to the changes of angle of attack
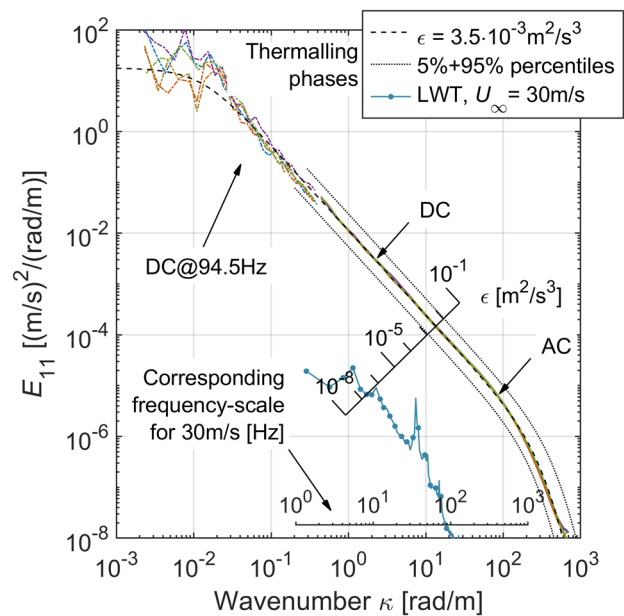
Fig. 18 Longitudinal spectra averaged over all thermalling phases of the five flights (solid lines, colour code see Fig. 22). Low wavenumber spectra (dashed dot lines) include motion of aircraft. Pope model spectra representing 5%, 50% and 95% percentiles of ε over all flights. Spectrum of LWT at 30 m/s (Romblad et al. 2022), corresponding to the average inflow speed in thermalling phases
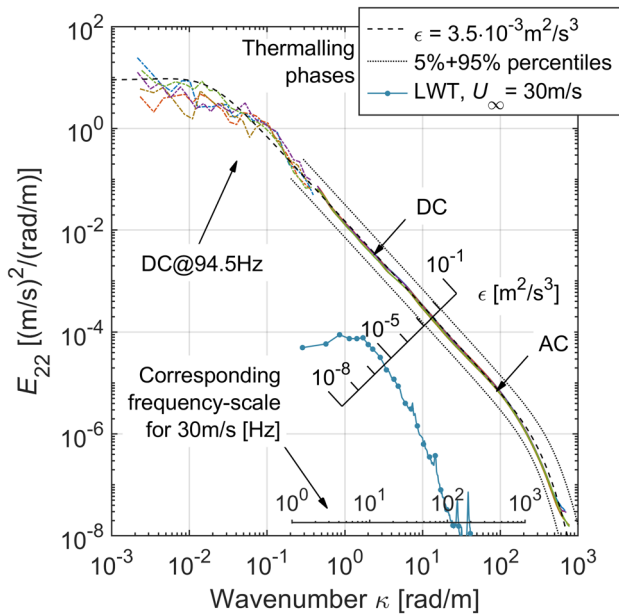
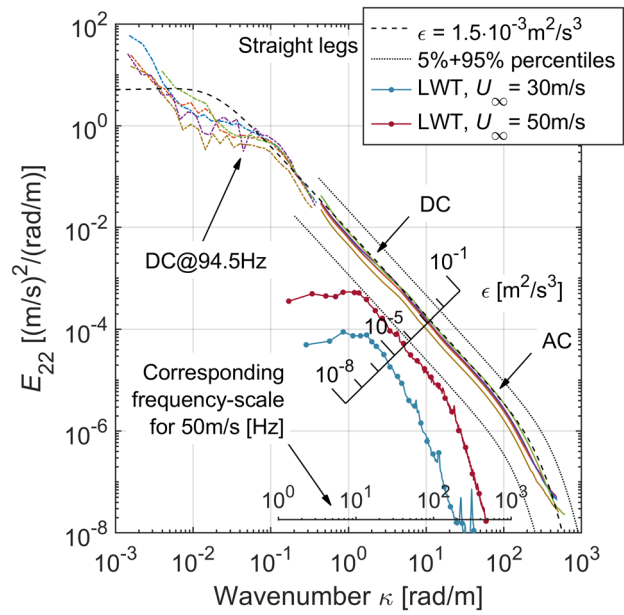**Fig. 19** Transversal spectra in thermalling phases, corresponding to Fig. 18

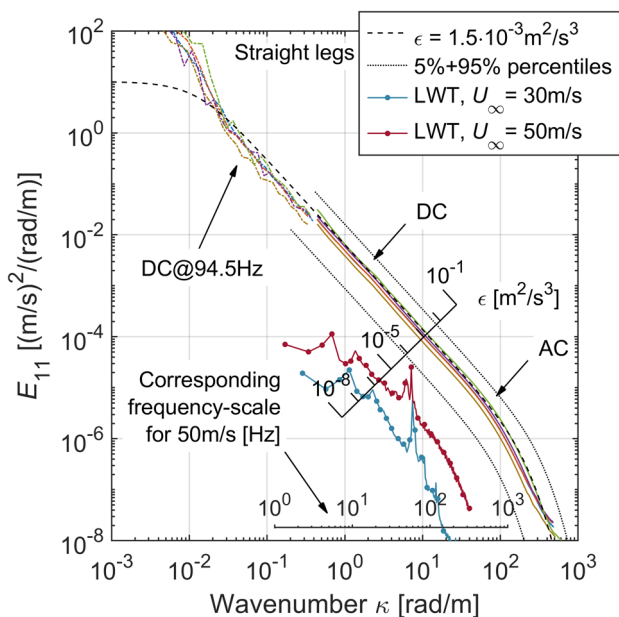**Fig. 21** Transversal spectra in straight legs, corresponding to Fig. 20

Fig. 20 Longitudinal spectra averaged over all straight legs of the five flights (solid lines, colour code see Fig. 22). Low wavenumber spectra (dashed dot lines) include motion of aircraft. Pope model spectra representing 5%, 50% and 95% percentiles of ε over all flights. Spectra of LWT at 30 m/s and at 50 m/s (Romblad et al. 2022), covering the range of typical inflow speeds in straight legs

Although the flights were conducted at different soaring conditions, their spectra collapse well, particularly the longitudinal spectra of the thermalling phases. The average spectra are accompanied by model spectra approximating the mean dissipation rate (thermalling phases: $3.5 \cdot 10^{-3}$ m^2/s^3; straight legs: $1.5 \cdot 10^{-3}$ m^2/s^3) and their 5% and 95% percentiles (thermalling phases: $1.2 \cdot 10^{-3}$ m^2/s^3 and $1.1 \cdot 10^{-2}$ m^2/s^3; straight legs: $7.6 \cdot 10^{-5}$ m^2/s^3 and $5.9 \cdot 10^{-3}$ m^2/s^3). For the model spectra Eq. 3, a kinematic viscosity ν of $1.7 \cdot 10^{-5}$ m^2/s and a lengthscale L of 150 m are used.

Figures 18, 19, 20 and 21 are complemented by spectra from x-wire measurements in the LWT (Romblad et al. 2022) for the range of inflow speeds in thermalling phases (30 m/s) and straight legs (30–50 m/s). These are clearly below the in-flight spectra, especially for the thermalling case. In this case and at frequencies of 0.2 kHz, the very low end of typical TS-frequencies for the present flight configurations, the spectra differ by a factor of $E_{11,\mathrm{flight}} / E_{11,\mathrm{LWT}} = 5000$, which corresponds to an amplitude ratio of $\sqrt{E_{11,\mathrm{flight}} / E_{11,\mathrm{LWT}}} = 70$.

As discussed in Sect. 3.1, local isotropy at small scales can be expected. In isotropic turbulence and in the inertial range the ratio between $E_{11}(\kappa)$ and $E_{22}(\kappa)$ theoretically takes the value of 0.75 (Pope 2000). Figure 22 presents the ratio $E_{11}(\kappa) / E_{22}(\kappa)$ averaged for all subsegments of each flight. For $\kappa = 0.5$ to 50 rad/m the ratio remains close to the theoretic value, but deviates on later flights, possibly indicating a degrading accuracy of the values derived in the pre-calibration. Above 30 rad/m, the ratio $E_{11}(\kappa) / E_{22}(\kappa)$ falls off
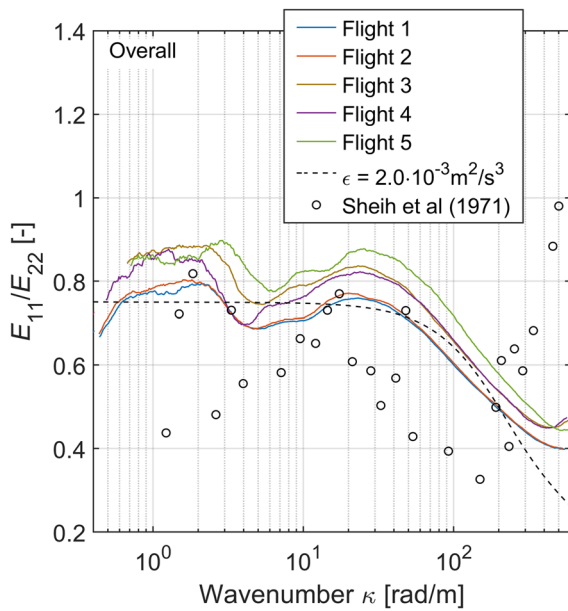
of the x-wires as the changes of the flight speed are larger during straight legs.

Fig. 22 Ratio of longitudinal and transversal spectra, averaged for the five flights, compared with theoretical value from Pope model spectrum. Symbols from Sheih et al. (1971)
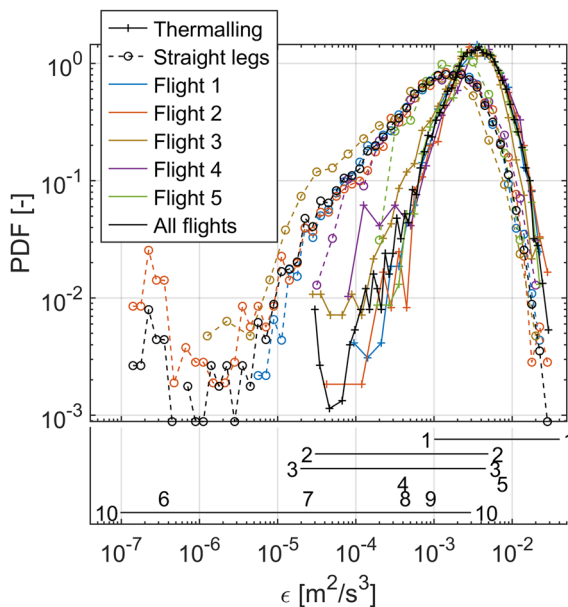

Fig. 23 PDFs of ε for thermalling phases (+) and straight legs (o) estimated for the individual flights and over all flights. Values from Literature for comparison: MacPherson and Isaac (1977): (1) in cumulus clouds, (2) between cumulus clouds; MacCready (1962): (3) soaring; Weissmüller (2011): (4) low turbulence, (5) moderate turbulence; Reeh (2014): (6) calm air, (7) light turbulence from thermal convection, (8) light turbulence from wind shear under stable conditions, (9) moderate turbulence from thermal convection; Guissart et al. (2021): (10) calm to moderately turbulent conditions

as it does in the model spectrum. For comparison, the data presented by Sheih et al. (1971) is plotted in Fig. 22. They attribute the scatter to experimental errors.

Figure 23 shows the PDF of the dissipation rates for thermalling phases and straight legs in comparison with dissipation rates obtained by other authors. In thermalling phases, there is only a small spread, ranging from what has been labelled "lightly turbulent" to "moderately turbulent". In contrast, the straight legs also include crossing of less turbulent air, thus stretching the distribution asymmetrically towards the low-ε end.

Section 3.3 showed that dissipation rates in thermalling phases seem to be log-normally distributed. This is not the case for the straight legs between thermals. We regard this as a key finding of this study, which has significant input on the simulation of FST in wind tunnel for applications related to the convective mixed layer. Especially the narrow range of dissipation rates found during thermalling allows a simplified mapping to these conditions, whereas the wide range of ε found during interthermal flight requires a more sophisticated approach. The latter one can take advantage of the PDFs presented in Fig. 23.

For the prediction of ε in the convective mixed layer of the atmosphere, the meteorological measures buoyancy flux and buoyancy parameter have been found appropriate (Kaimal and Finnigan 1994). However, for the purpose of testing airfoils for sailplane applications, it is useful to discuss the relationship of ε with metrics, which are essential in the modelling of cross-country flights, and which can be obtained from flight records, such as altitude, time of day or vertical air velocity. Certainly, the results of this study are based on a limited set of data and are only applicable to comparable weather situations in similar climatic regions.

The dissipation rate does not show a recognisable trend with respect to the relative altitude, from ground to the usable upper end of the thermals. The latter is estimated from an envelope of the maximum altitudes reached. This result agrees with Caughey and Palmer (1979), showing a constant dissipation rate throughout most of the vertical extend of the convective mixed layer.

Figure 24 shows the dissipation rate versus the time of day. In this figure, and in Fig. 25, every dot represents a subsegment of the flights. The time is normalised to range from sunrise to sunset. This is a rough model, as begin and end of thermal activity depends on additional meteorological factors. The diurnal pattern of convective activity is not to be described with these few data, only the remark is made that low dissipation rates were only found either early or at times so late that they show no more use of thermals in circling flight. This is in line with the observation that turbulent kinetic energy decreases in the afternoon when the surface buoyancy flux decays (Darbieu et al. 2015).
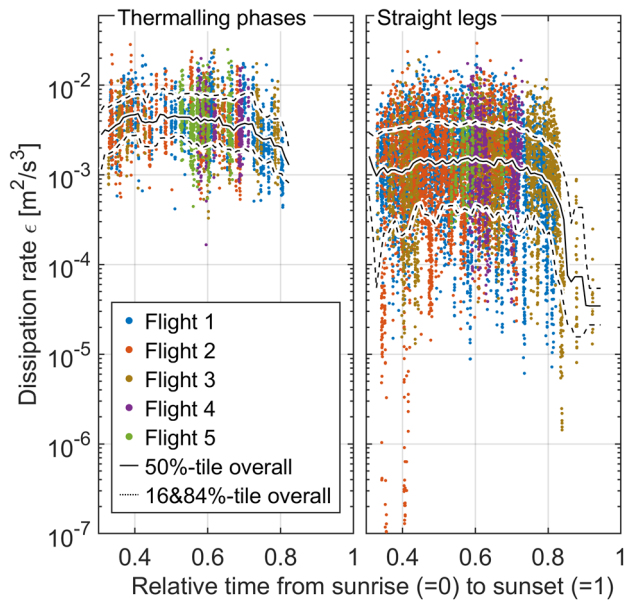
Fig. 24 Relation between time of day and ε. Time in relation to the span between sunrise and sunset. Every dot represents a 4 s subsegment. 16% and 84% percentile comparable to one standard deviation in a normal distribution
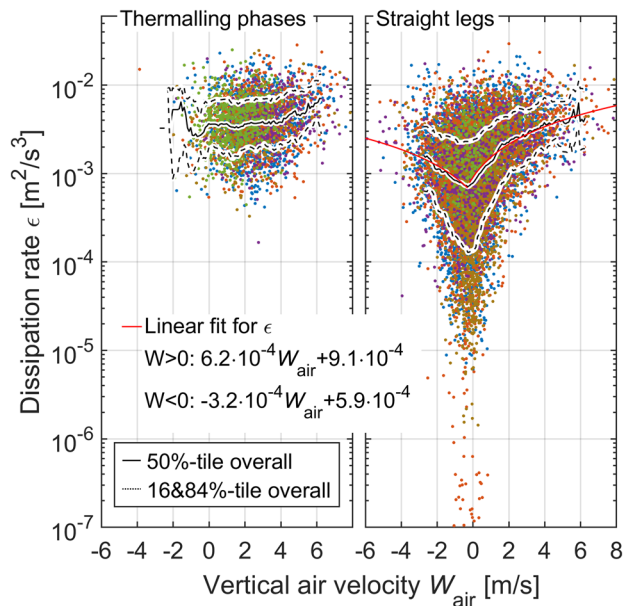

Fig. 25 Relation between vertical air velocity W_{air} and ε. Every dot represents a 4 s subsegment. Colour code as in Fig. 24. Linear fit between ε and W_{air}
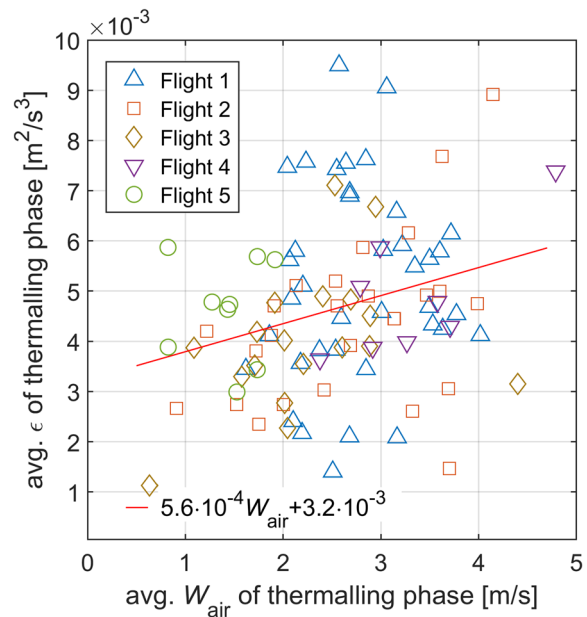
Fig. 26 Relation between vertical air velocity W_{air} and ε, both averaged over each thermalling phase

found for both, raising and sinking air. The difference may stem from the fact that updrafts are closer to the source of convective energy than downdrafts. However, these relations are certainly a question of how often which kind of air mass was crossed. The plot for thermalling phases does not show such a comprehensive trend, although for $W_{air} > 4$ m/s there is a slope comparable with the straight legs. However, not only is W_{air} in a dynamic environment, like a thermal, insufficiently resolved by the system, moreover, transient vertical velocities close to zero are not a measure for the absence of turbulence. Therefore, Fig. 26 plots integral values of W_{air} and ε, each symbol representing the average over one thermal. There is considerable scatter, but again a linear least square fit yields a slope of $d\varepsilon/dW_{air} \approx 6 \cdot 10^{-4}$ m/s^2.

The aim of this study is to provide a basis for the simulation of turbulence in wind tunnel experiments, e.g. by using passive grids for smaller scales (Romblad et al. 2022) and active grids (Wester et al. 2022) for larger scales. However, the following limitations should be noted: First, Guissart et al. (2021) have shown that in free flight and in the wind tunnel, with apparently similar FST at the relevant scales, the results, e.g. the transition location, still can be different. Second, the measurements of this study were not carried out under predefined traversing strategies, i.e. the active guidance of the pilots is embedded in the data. This applies all the more to the straight legs, in which completely different types of air masses are crossed according to the pilots' decisions. It must be recognised that data from this study reflect the Central European convective mixed layer from the perspective of a cross-country flying sailplane.

Figure 25 shows the dissipation rate versus the vertical air velocity W_{air}. The plot for straight legs shows that low dissipation rates can only be found in air masses with small W_{air}. A linear trend with the 50% percentile curve can be

4 Conclusion

NFL-airfoils are state of the art for general aviation and wind turbines. To regard the operational inflow conditions during the design process, it requires to characterise the FST under the intended operation. This study focuses on cross-country flights of sailplanes, i.e. on one hand on the convective mixed layer of the atmosphere, on the other hand on the specific flight phases that are associated with cross-country flights, namely circling in thermals and straight legs between thermals. For this purpose, the longitudinal u and transversal v velocities were recorded with a CTA x-wire-probe during cross-country flights, continuously up to 9 h. Additionally, environmental data (temperature, relative humidity, static and dynamic pressure) and supplemental data (GPS-flight path, probe accelerations) were recorded to get an accurate picture of the flight profile and to support the postprocessing. Twenty-two hours of flight time were included in the analyses, covering Central European soaring weather conditions, with average vertical air velocities of 1.5 to over 3.5 m/s. The evaluation of such long CTA measurements requires the compensation of varying temperature and air density as well as the cross-check with the inflow speed from dynamic pressure. This revealed that the effective temperature of the x-wires cannot be assumed to be constant over several hours. However, without an accurate supplementary inflow angle measurement, it is not possible to determine directly the specific correction of each wire. An approach was developed that uses the assumption of isotropy at small scales to determine the appropriate values of the effective wire temperatures.

Because of the instationary flight conditions, it was not possible to determine either the integral lengthscale nor the Taylor microscale. The Kolmogorov scale η is found to be close to log-normal distributed in thermalling phases, with a mean value of about 1.1 mm, whereas in the straight legs, the PDFs of η do not show a comparable uniformity.

Several predictions of Kolmogorov's inertial range theories concerning the velocity derivatives $\partial u'/\partial x$ and $\partial v'/\partial x$ can be confirmed. The RMS value of $\partial u'/\partial x$ scales with $\varepsilon^{1/3}$ and with the spatial scale $r^{-2/3}$. In the inertial range, the skewness $S_{u,c}$ of $\partial u'/\partial x$ is nearly constant at a value of 0.24 and thus independent of the level of turbulence and of $(\kappa\eta)_c$ (cf. Sukoriansky et al. 2018), whereas the kurtosis $K_{u,c}$ of $\partial u'/\partial x$ shows a slope of $(\kappa\eta)_c^{0.1}$, which is consistent with the expected relationship to the spatial scale r (cf. Sreenivasan and Antonia 1997).

In thermalling phases, the FST can well be characterised, and ε shows little spread within and between the different flights. The turbulence in thermalling phases shows a log-normal distribution. Over all thermalling phases, the dissipation rate averages $3.5 \cdot 10^{-3}$ m^2/s^3, with a narrow spread of 1.2·10^{-3} to 1.1·10^{-2} m^2/s^3 (5% and 95% percentiles). This is considerably higher than at the LWT, e.g. the longitudinal spectrum in thermalling phases at 0.2 kHz is 37 dB higher than in the LWT for a comparable speed (30 m/s).

For the straight legs, no uniform description of turbulence could be found. The probability distribution of ε does not have a standardised shape, but depends on the air mass crossed by the glider, like, e.g. areas with little convection. Therefore, values of ε lower than in thermalling phases occur. Very low values of ε, as, e.g. below $5 \cdot 10^{-6}$ m^2/s^3, however, are not observed during the thermally active period of the day. As predicted by the meteorological model the altitude shows no evident influence on ε in the convective mixed layer. However, both in straight legs and in thermalling phases, a linear trend of ε with respect to the vertical air velocity is found.

For the transfer into wind tunnel experiments, it should be noted that the processed results of this study are of course a function of the pilots' flight strategies and therefore represent only a biased statistics of the convective boundary layer.

Declarations

Conflict of interest The authors have no relevant financial or non-financial interests to disclose.

References

Arnal D (1992) Boundary layer transition: prediction, application to drag reduction. In: Special course on skin friction drag reduction, AGARD report 786

Arntz KD (1991) Flugmessung zur Ermittlung von Druck- und Geschwindigkeitsschwankungen in der Atmosphäre mit der LFU-205. Technische Universität Braunschweig, Studienarbeit

Balzer W, Fasel HF (2016) Numerical investigation of the role of free-stream turbulence in boundary-layer separation. J Fluid Mech 801:289–321. https://doi.org/10.1017/jfm.2016.424

Batchelor GK, Townsend AA (1947) Decay of vorticity in isotropic turbulence. Proc R Soc A Math Phys Eng Sci 190(1023):534–550. https://doi.org/10.1098/rspa.1947.0095

Baumann M (2013) Manual of the system low-noise miniature CTA System. Ingenieurbüro Dr. Baumann

Bendat J, Piersol A (2010) Random data analysis and measurement procedures, 4th edn. Wiley, Hoboken, NJ

Bertolotti FP (2001) Effect of atmospheric turbulence on a laminar boundary-layer. Tech Soar 25:154–159

Boiko AV, Grek GR, Dovgal AV, Kozlov VV (2002) The origin of turbulence in near-wall flows, Springer, Berlin, Heidelberg, chap 5 Laminar-turbulent transition at high free-stream turbulence level

Bourdopoulos GI, Pnevmatikakis A, Anastassopoulos V, Deliyannis T (2003) Delta-sigma modulators: modeling, design and applications. Imperial College Press, London

Bruun HH (1995) Hot-wire anemometry: principles and signal analysis. Oxford University Press

Burattini P, Lavoie P, Antonia RA (2008) Velocity derivative skewness in isotropic turbulence and its measurement with hot wires. Exp Fluids 45(3):523–535. https://doi.org/10.1007/s00348-008-0495-3

Caughey SJ, Palmer SG (1979) Some aspects of turbulence structure through the depth of the convective boundary layer. Q J R Meteorol Soc 105:811–827. https://doi.org/10.1002/qj.49710544606

Crouch JD (2008) Modeling transition physics for laminar flow control In: 38th AIAA fluid dynamics conference, AIAA, 2008–3832. https://doi.org/10.2514/6.2008-3832

Darbieu C, Lohou F, Lothon M, Vilà-Guerau de Arellano J, Couvreux F, Durand P, Pino D, Patton EG, Nilsson E, Blay-Carreras E, Gioli B (2015) Turbulence vertical structure of the boundary layer during the afternoon transition. Atmos Chem Phys 15:10071–10086. https://doi.org/10.5194/acp-15-10071-2015

Djenidi L, Antonia RA (2012) A spectral chart method for estimating the mean turbulent kinetic energy dissipation rate. Exp Fluids 53(4):1005–1013. https://doi.org/10.1007/s00348-012-1337-x

Drela M (1989) XFOIL: an analysis and design system for low Reynolds number airfoils. In: Mueller TJ (ed) Low Reynolds number aerodynamics. Springer, Berlin Heidelberg. https://doi.org/10.1007/978-3-642-84010-4_1

Freymuth P, Fingerson L (1997) Hot-wire anemometry at very high frequencies: effect of electronic noise. Meas Sci Technol 8:115–116. https://doi.org/10.1088/0957-0233/8/2/001

Guissart A, Romblad J, Nemitz T, Tropea C (2021) Small-scale atmospheric turbulence and its impact on laminar-to-turbulent transition. AIAA J 59(9):3611–3621. https://doi.org/10.2514/1.J060068

Hultmark M, Smits AJ (2010) Temperature corrections for constant temperature and constant current hot-wire anemometers. Meas Sci Technol 21:105404. https://doi.org/10.1088/0957-0233/21/10/105404

Kaimal JC, Finnigan JJ (1994) Atmospheric boundary layer flow. Oxford University Press, New York

Kannuluik WG, Carman EH (1951) The temperature dependence of the thermal conductivity of air. Aust J Sci Res A Phys Sci 4:305–314. https://doi.org/10.1071/CH9510305

Kendall J (1997) Experiments on boundary-layer receptivity to freestream turbulence. In 36th AIAA aerospace sciences meeting and exhibit. https://doi.org/10.2514/6.1998-530

Kolmogorov AN (1941) The local structure of turbulence in incompressible viscous fluid for very large Reynolds numbers. Cr Acad Sci URSS 30:301–305. https://doi.org/10.1098/rspa.1991.0075

Kolmogorov AN (1962) A refinement of previous hypotheses concerning the local structure of turbulence in a viscous incompressible fluid at high Reynolds number. J Fluid Mech 13:82–85. https://doi.org/10.1017/S0022112062000518

Kraichnan RH (1974) On Kolmogorov's inertial-range theories. J Fluid Mech 62(2):305–330. https://doi.org/10.1017/S002211207400070X

Küssner G (1932) Beanspruchung von Flugzeugflügeln durch Böen, Z Flugtechn Motorluftschiffahrt, Oct 1931: 589–586, 605–515. engl transl in NACA TM 654, https://ntrs.nasa.gov/api/citations/19930094762/downloads/19930094762.pdf

MacCready PB (1962) Turbulence measurements by sailplane. J Geophys Res 67:1041–1050. https://doi.org/10.1029/JZ067i003p01041

Mack LM (1977) Transition and laminar instability. Jet Propuls Lab Publication, pp 77–15

MacPherson JI, Isaac GA (1977) Turbulent characteristics of some Canadian cumulus clouds. J Appl Meteor 16:81–90. https://doi.org/10.1175/1520-0450(1977)016%3c0081:TCOSCC%3e2.0.CO;2

Maughmer MD, Coder JG, Wannenmacher C, Würz W (2017) The design of a new racing sailplane: a new thermal mix model and the role of transitional CFD, In: 17th AIAA aviation technology, integration, and operations conference. https://doi.org/10.2514/6.2017-4091

Miley SJ, Horstmann KH (1991) Data report of flight and wind tunnel investigations of Tollmien-Schlichting waves on an aircraft wing, part I, report IB 129–91/18, Institute for Design Aerodynamics, DLR, Braunschweig

Morkovin MV (1969) On the many faces of transition. In: Wells CS (ed) Viscous drag reduction. Plenum, New York, pp 1–31. https://doi.org/10.1007/978-1-4899-5579-1_1

Nobach H, Tropea C (2012) A statistical method for transforming temporal correlation functions from one-point measurements into spatial and spatiotemporal statistics. Exp Fluids 53(6):1815–1821. https://doi.org/10.1007/s00348-012-1392-3

Obukhov AM (1962) Some specific features of atmospheric turbulence. J Fluid Mech 13:77–81. https://doi.org/10.1017/S0022112062000506

Oolman, L (2021), Wyoming Weather Web, University of Wyoming, http://weather.uwyo.edu/upperair/sounding.html. Accessed 1 Aug 2021

Pätzold F (2018) Windmessung mittels Segelflugzeug, Dissertation, Technische Universität Braunschweig. https://publikationsserver.tu-braunschweig.de/servlets/MCRFileNodeServlet/dbbs_derivate_00044501/Diss_Paetzold_Falk.pdf

Pearson JM, Sharman RD (2017) Prediction of energy dissipation rates for aviation turbulence. Part II: nowcasting convective and non-convective turbulence. J Appl Meteorol Climatol 56(2):339–351. https://doi.org/10.1175/JAMC-D-16-0312.1

Peltzer I (2008) Comparative in-flight and wind tunnel investigation of the development of natural and controlled disturbances in the laminar boundary layer of an airfoil. Exp Fluids 44:961–972. https://doi.org/10.1007/s00348-007-0455-3

Pope SB (2000) Turbulent flows. Cambridge University Press, Cambridge

Reeh AD (2014) Natural laminar flow airfoil behavior in cruise flight through atmospheric turbulence. Dissertation, Technische Universität Darmstadt. https://tuprints.ulb.tu-darmstadt.de/id/eprint/4123

Rhyne RH, Steiner R (1964), Power spectral measurement of atmospheric turbulence in severe storms and cumulus clouds, Technical Report, NASA-TN-D-2469. https://ntrs.nasa.gov/api/citations/19640021084/downloads/19640021084.pdf

Richardson LF (1922) Weather prediction by numerical process. Cambridge University Press

Riedel H, Sitzmann M (1998) In-flight investigations of atmospheric turbulence. Aerosp Sci Technol 2:301–319. https://doi.org/10.1016/S1270-9638(98)80007-2

Romano GP, Ouellette NT, Xu H, Bodenschatz E, Steinberg V, Meneveau C, Katz J (2007) Measurements of turbulent flows. In: Tropea C, Yarin A, Foss JF (eds) Springer handbook of experimental fluid dynamics. Springer, Berlin Heidelberg. https://doi.org/10.1007/978-3-540-30299-5_10

Romblad J, Ohno D, Nemitz T, Würz W, Krämer E (2018) Laminar to turbulent transition due to unsteady inflow conditions: wind tunnel experiments at increased turbulence levels. Deutsche Gesellschaft für Luft-und Raumfahrt-Lilienthal-Oberth eV. https://doi.org/10.25967/480138

Romblad J, Greiner M, Guissart A, Würz W (2022) Characterisation of low levels of turbulence generated by grids in the settling chamber of a laminar wind tunnel. Exp Fluids 63:65. https://doi.org/10.1007/s00348-022-03418-5

Saric WS, Reed HL, Kerschen EJ (2002) Boundary-layer receptivity to freestream disturbances. Annu Rev Fluid Mech 34(1):291–319. https://doi.org/10.1146/annurev.fluid.34.082701.161921

Sharman R (2016) Nature of aviation turbulence. In: Sharman R, Lane T (eds) Aviation turbulence. Springer, Berlin, Heidelberg. https://doi.org/10.1007/978-3-319-23630-8

Sheih CM, Tennekes H, Lumley JL (1971) Airborne measurement of the small-scale structure of atmospheric turbulence. Phys Fluids 201(14):201–215. https://doi.org/10.1063/1.1693416

Smith AMO, Gamberoni N (1956) Transition, pressure gradient and stability theory. Douglas Aircr Co, Rep ES 26388

Sreenivasan KR, Antonia RA (1997) The phenomenology of small-scale turbulence. Annu Rev Fluid Mech 29:435–472. https://doi.org/10.1146/annurev.fluid.29.1.435

Sukoriansky S, Kit E, Zemach E, Midya S, Fernando HJS (2018) Inertial range skewness of the longitudinal velocity derivative in locally isotropic turbulence. Phys Rev Fluids 3:114605. https://doi.org/10.1103/PhysRevFluids.3.114605

Taylor GI (1938) Production and dissipation of vorticity in a turbulent fluid. Proc R Soc A Math Phys Eng Sci 164(916):15–23. https://doi.org/10.1098/rspa.1938.0002

Tennekes H (1968) Simple model for the small-scale structure of turbulence. Phys Fluids 11:669. https://doi.org/10.1063/1.1691966

van Ingen JL (1956) A suggested semi-empirical method for the calculation of the boundary layer transition region. Tech Hogesch. Delft, Vliegtuigbouwkunde, Rapp VTH-74. http://resolver.tudelft.nl/uuid:cff1fb47-883f-4cdc-ad07-07d264f3fd10

van Ingen JL (1977) Transition, pressure gradient, suction, separation and stability theory. In: AGARD CP-224

Weismüller M (2011) A new approach to aerodynamic performance of aircraft under turbulent atmospheric conditions. Dissertation, Technische Universität Darmstadt. https://tuprints.ulb.tu-darmstadt.de/id/eprint/2934

Wester TTB, Krauss J, Neuhaus L, Hölling A, Gülker G, Hölling M, Peinke J (2022) How to design a 2D active grid for dynamic inflow modulation. Flow Turbul Combust 108:955–972. https://doi.org/10.1007/s10494-021-00312-8

Wildmann N, Eckert R, Dörnbrack A, Gisinger S, Rapp M, Ohlmann K, van Niekerk A (2021) In situ measurements of wind and turbulence by a motor glider in the Andes. J Atmos Ocean Technol 38(4):921–935. https://doi.org/10.1175/JTECH-D-20-0137.1

Wortmann FX, Althaus D (1964) Der Laminarwindkanal des Instituts für Aero- und Gasdynamik an der technischen Hochschule Stuttgart. Z Flugwiss 12(4):129–134

Wyngaard JC, Tennekes H (1962) Measurements of the small-scale structure of turbulence at moderate Reynolds numbers. Phys Fluids 13:1962–1969. https://doi.org/10.1063/1.1693192

Zanin BY (1985) Transition at natural conditions and comparison with the results of wind tunnel studies. In: Kozlov VV (ed) Laminar-turbulent transition. International Union of Theoretical and Applied Mechanics. Springer, Berlin, Heidelberg. https://doi.org/10.1007/978-3-642-82462-3_67

Zhu Y, Antonia RA (1996) The spatial resolution of hot-wire arrays for the measurement of small-scale turbulence. Meas Sci Technol 7:1349–1359. https://doi.org/10.1088/0957-0233/7/10/006